Chemical compression and ferroic orders in La substituted math xmlns="http://www.w3.org/1998/Math/MathML">mrow>mi >BiFe/mi>msub>mi mathvariant="normal">O/mi> mn>3/mn>/msub>/mrow>/math>

Valeri Petkov, Adeel Zafar, Peter Kenesei, and Sarvjit Shastri

Phys. Rev. Materials **7**, 054404 — Published 26 May 2023

DOI: 10.1103/PhysRevMaterials.7.054404

Chemical compression and ferroic orders in La substituted $BiFeO_3$

V. Petkov[1], A. Zafar[1] and S. Shastri[2]
[1]Department of Physics, Central Michigan University, Mt. Pleasant, Michigan 48858, USA
[2]X-ray Science Division, Advanced Photon Source, Argonne National Laboratory, Argonne, IL 60439, USA

Abstract

Chemical compression effects on the ferroic orders in La substituted $BiFeO_3$ are studied by atomic pair distribution function analysis and structure modeling. While rhombohedral $BiFeO_3$ exhibits ferroelectricity and antiferromagnetism (AF) with a cycloidal Fe spin arrangement leading to zero magnetization, La substituted $BiFeO_3$ exhibits a reduced lattice polarization, strengthened AF order and apparently suppressed spin cycloid leading to nonzero magnetization. The observed changes in the ferroic orders arise from the chemical compression induced changes in the octahedral rotation and ferrolectric displacement of Bi atoms, which appear as lattice degrees of freedom entangling the electronic and magnetic orders in $BiFeO_3$.

1. Introduction

There is an increased interest in strongly correlated materials that exhibit coupled electronic, magnetic and lattice degrees of freedom leading to fascinating physics and practical applications [1-5]. Among those materials, the multiferroic $BiFeO_3$ (BFO) is unique because it exhibits spontaneous ferroelectric (Curie temperature T_c = 1033 K) and antiferromagnetic (Neel temperature T_N = 643 K) orders over a broad temperature range while adopting the same rhombohedral Space Group (S.G.) *R3c* structure [6-11], providing an opportunity to control the electric properties by magnetic field, and vice versa. The structure features a perovskite-type lattice of corner sharing Fe-O_6 octahedra with Bi atoms occupying the cavities between the octahedra (Figure 1*a*). Contrary to the aristotype cubic perovskite, the octahedra in BFO are rotated in an antiferrodistortive manner about the polar $<111>_R$ axis in the rhombohedral (R) lattice. Both Fe and Bi atoms are shifted from their position in the cubic lattice along $<111>_R$, giving rise to distinct short (1.97 Å) and long (2.12 Å) Fe-O bonding distances and a broad distribution of Bi-O distances, ranging about 2.25 Å - 3.5 Å [12-14]. The largely ionic bonding between Fe^{3+}/Bi^{+3} and O^{-2} ions has a partial covalent character, where oxygen atoms are bonded by O*p* states to both Bi and Fe, providing a link between the A and B sites of the perovskite ABO_3 lattice. Indeed, it is the asymmetric covalent bond-like interaction between the lone pair of Bi $6s^2$ and O *2p* orbitals what is considered to be behind the ferroelectricity in BFO. Notably, because the Fe-O-Fe bond angle appears close to 155°, the superexchange interaction between Fe magnetic moments is antiferromagnetic (AF) in character. Furthermore, due to Dzyaloshinskii-Moriya (DM) interactions, the Fe moments are also weakly canted away from the AF lattices, resulting in a weak magnetization. However, superimposed on the AF ordering, there is cycloidal spin structure arrangement with a period of about 62 nm, leading to a cancellation of the macroscopic magnetization over a single period of the cycloid. The presence of a spin cycloid and related zero magnetization inhibits the

linear magnetoelectric (ME) coupling effect in BFO, thus hampering its usage in practical applications [15-19].

A lot of effort has been put into finding an efficient way to improve the ME coupling in bulk BFO through suppressing the cycloidal spin order and thus producing nonzero magnetization while disturbing the ferroelectric order as little as possible. It has been found that the cycloid can be suppressed by an application of strong magnetic field [20], reducing BFO to nanosized dimensions [21] or selective chemical substitution of Bi atoms in the perovskite lattice. Among the many types of substitution under investigation, those involving light rare earth metals have shown a great promise [22-30]. A typical example is La substituted BFO, where both the emergence of macroscopic magnetization and an apparent increase in the saturation and remnant ferroelectric polarization is observed [31-38]. The driving forces behind the positive effect of La substitution for Bi are, however, still ambiguous. The situation is exacerbated by difficulties in determining the structure type for rare earth substituted BFO in general and in particular for La substituted BFO, and, hence, ascertaining the presence or absence of an atomic structure state conducive to a ferroelectric order and non-zero magnetization. More specifically, several studies have suggested that BFO exhibits a sequence of phase transitions with the La substitution, including from a polar S.G. *R3c* to polar S. G. *C222* or polar S.G. *P1* structure [39], followed by a transition to polar S.G. $Pna2_1$, nonpolar S.G. *Imma* or nonpolar S.G. *Pbnm* structure, where the nonpolar structures cannot harbor ferroelectric order [40,41]. Extended composition ranges of a phase segregation and the emergence of incommensurate polar S. G. $Pn2_1a(00\gamma)000$ and non-polar S.G. $Imma(00\gamma)s00$ structures at particular La concentrations have also been suggested [36,42-44]. Here we are addressing this ambiguity by employing total and resonant x-ray scattering coupled to structure modeling to study the effect of La substitution on the atomic arrangement in BFO, including the local lattice symmetry and ferroelectric polarization. Magnetic measurements are done to quantify the changes in the AF order. We find that, though modified, the ferroelectric displacement of Bi atoms and rhombohedral symmetry of the parent BFO survive in $Bi_{1-x}La_xFeO_3$ to a high level of La substitution ($x \leq 0.4$) and, though diminished, the lattice polarization also survives. We also find that La substitution strengthens the AF order and suppresses the spin cycloid, releasing a weak canted magnetic moment that contributes to the concurrent emergence of macroscopic magnetization and observed enhancement in the ME coupling.

1. Experimental

1.1 Sample preparation

Polycrystalline $Bi_{1-x}La_xFeO_3$ samples, where x=0, 0.1, 0.2, 0.3 and 0.4, were prepared by a traditional solid state synthesis where stoichiometric amounts of Bi_2O_3 (99.999 %), Fe_2O_3 (99.999 %) and La (99.9 %) were intermixed, thoroughly grinded, calcined at 1270 K and then annealed at 980 K. Powder diffraction patterns

for the samples were obtained on a Panalytical diffractometer using Mo K_α radiation and a secondary monochromator to record high-resolution Bragg peaks. The patterns are shown in Figure 1(*b*).

1.2 Magnetic properties characterization

Magnetic properties of the samples were studied on a Physical property measuring system (PPMS) at room temperature. Experimental hysteresis curves are summarized in Figure 1(*c*). As expected, pure BFO does not show any magnetic hysteresis, which is typical for AF materials. The samples containing La show magnetic hysteresis with a significant remanent magnetization. The result confirms the spin cycloid in La substituted BFO is increasingly suppressed with La content.

1.3 Total x-ray scattering experiments

Total x-ray scattering experiments were conducted at the beamline 1-ID, Argonne National Laboratory using x-rays with energy of 90.500 keV (λ=0.1368 Å). Higher energy x-rays were used to reach high wave vectors, which is essential for obtaining high-resolution atomic pair distribution functions (PDFs). Samples were packed in thin walled Kapton tubes with a diameter of 0.3 mm to minimize the absorption of x-rays in the samples. Scattered intensities were recorded with a single-photon-counting Pilatus detector up to wave vectors q_{max} of 26 $Å^{-1}$. Using the software PDFgetX3 [45], the intensities were reduced to total PDFs $G(r)=4\pi r[\rho(r)-\rho_o]$, where $\rho(r)$ and ρ_o are the local and average atomic number density, respectively, and r is the radial distance. As shown in Figure 1(*d*), the PDFs exhibit a series of well-defined peaks, reflecting the well-defined atomic arrangement in pure and La substituted BFO. The position of the peaks directly corresponds to frequently occurring atomic pair distances and the area of the peaks reflects the number of atomic pairs at those distances. Notably, atomic PDFs take into account both the Bragg peaks and diffuse component of the diffraction data and, hence, are sensitive to both the average crystal structure and local deviations from it, including lattice distortions in perovskites arising from chemical substitution [46,47]. As can also be seen in the Figure, the PDFs change systematically with La content, indicating that, even though La is barely different from Bi in size (1.38 Å for Bi vs 1.36 Å for La for 12-fold oxygen coordination), La substitution modifies the crystal structure of BFO significantly.

1.4 Resonant total x-ray scattering at the K edge of Bi

The total PDFs for pure and La substituted BFO shown in Figure 1(*d*) reflect all correlations between the constituent atoms. In the case of BFO, those are Bi-Bi, Bi-Fe, Bi-O, Fe-Fe, Fe-O and O-O pair correlations. As can be seen in Figure 2(*a*), the correlations appear as heavily overlapping peaks, making it difficult to interpret the PDF data unambiguously. To obtain structure data with an increased sensitivity to atomic correlations involving the ferroactive Bi atoms, we conducted a resonant total x-ray scattering experiment at the K edge of Bi (95.5124 keV). The scattered intensities were collected using a Pilatus detector, where its threshold voltage was adjusted to remove the unwanted sample environment and fluorescent scattering from the samples as much as possible. Because of their superb energy resolution, it has been a common

practice to employ Ge solid state detectors in resonant scattering experiments. The dynamic range and data collection time for Ge detector are, however, much inferior to those of 2D Pilatus detectors, prompting us opt for the latter. The experiments involved collecting two data sets for each sample up to wave vectors q_{max} of 26 $Å^{-1}$, where the first set was collected using x rays with energy 25 eV below the K edge of Bi and the second one was collected using x-ray with energy 500 eV below that edge (Fig. 2*b*). The intensity difference between the data sets (Fig. 2*c*) comes from differences in the atomic scattering factors of Bi atoms for the two energies, which largely arise from differences in the so-called dispersion corrections *f'* and *f''* to the factors. The Fourier transform of the intensity difference, known as a Bi-differential PDF, reflects only correlations involving Bi atoms, that is, only Bi-Bi, Bi-Fe and Bi-O correlations in the case of pure BFO, providing an extra, chemistry-specific data set for the structure modeling described below (see Fig. S1 in Supplemental Material [48]). Using the respective intensity differences, experimental Bi-differential PDFs for the studied La substituted BFO samples were computed with the help of an improved version of the software RAD [49]. The PDFs are shown in Fig. 2(*d*). The unknown values for *f'* and *f''* needed in the derivation of Bi-differential PDFs were determined by measuring the absorption of BFO sample over an energy range extending from 86 keV to 96 keV, normalizing the absorption against *f''* and using the Kramers-Kronig relationship to compute *f'* from *f''*. More details about resonant x-ray scattering experiments aimed at derivation of differential atomic PDFs can be found in refs. [50-52].

2. Diffraction data analysis and 3D structure Modeling

2.1 Average crystal structure

To ascertain the average crystal structure of La substituted BFO, we carried out Rietveld analysis of the in-house XRD patterns. The analysis was performed using the software Fullprof [53]. At first, the XRD patterns were fit with a model based on the rhombohedral S. G. *R3c* type structure. As expected, the model reproduced very well the XRD pattern for pure BFO (Fig. S2 [48]). It fit reasonably well the XRD patterns for $Bi_{1-x}La_xFeO_3$ samples with low La content (x=0.1 and x=0.2; Fig. 3*a,b*) but failed to reproduce the XRD patterns for $Bi_{0.7}La_{0.3}FeO_3$ and $Bi_{0.6}La_{0.4}FeO_3$ (Figures 3*c,d*). Other, frequently considered structure types, including S.G. *C222*, S.G. *Pna2₁*, S.G. *Pbnm, S.G. Cc, SG. Cm* and S.G. *Imma* structure types, were also tested against the XRD patters for the latter two samples. The models performed worse, as shown in Figure S3. This prompted us to attempt a triclinically distorted rhombohedral model with a S.G. *P1* symmetry that has been found useful in describing the structure of pure BFO [54]. The S.G. *P1* model we considered is a variant of the S.G. *R3c* structure model of pure BFO where the three lattice parameters and rhombohedral angles are decoupled while the rhombohedral symmetry relationship between the atomic sites is left intact. It has 14 refinable parameters (vs 10 for the S.G. *R3c* model; see Table S1 [48]) and reproduces very well not only the XRD data for $Bi_{0.9}La_{0.1}FeO_3$ and $Bi_{0.8}La_{0.2}FeO_3$ (Fig. S4 [48]) but also those for $Bi_{0.7}La_{0.3}FeO_3$

and $Bi_{0.6}La_{0.4}FeO_3$ (Figure 4), indicating that the replacement of Bi with the smaller in size La induces an overall distortion of the rhombohedral crystal lattice in BFO.

2.2 Local crystal structure

To determine the local structure of La substituted BFO, we fit the experimental total PDFs G(r) with the structure models explored by Rietveld analysis. The fits were done with the help of the software PDFgui [55], where the so-called instrumental resolution parameters q_{damp} and q_{broad} were given values of 0.013 and 0.023 determined by measuring and analyzing a Si powder standard. As shown in previous studies [21] and confirmed here (Fig. S2 [48]), the atomic PDF for pure BFO can be well fit with a model based on the rhombohedral S.G. *R3c* structure type, which also fits well the XRD data for BFO. The model appeared less successful for the La doped samples, where several other structure types were also tested. Similarly to the case of Rietveld analysis of XRD data, models based on S.G. *C222*, S.G. *Pna2₁*, S.G. *Pbnm, S.G. Cc, SG. Cm* and S.G. *Imma* type structures failed to reproduce well the experimental PDF data for the La substituted samples, as exemplified in Fig. S5 [48]. Again, similarly to the case of Rietveld analysis of XRD data, the triclinically distorted rhombohedral model (S.G. *P1*) well reproduced the experimental PDF data for all La substituted samples (Figure 5). Models based on the S.G. *C222*, S.G. *Pna2₁*, S.G. *Pbnm, S.G. Cc, SG. Cm* and S.G. *Imma* structure types where the lattice parameters and angles are decoupled did not refine well against the PDF data for the La substituted samples. The results indicate that not only on average but also locally pure rhombohedral BFO and La $Bi_{1-x}La_xFeO_3$, where $x<0.4$, share significant structural similarities. The PDF refined lattice parameters for pure BFO (S.G. *R3c* lattice symmetry) and La substituted BFO samples (S.G. *P1* lattice symmetry) are summarized in Table S2 [48]. The Rietveld, PDF refined lattice parameters (see Table S2 [48]) and computed from them average atomic volume in the La substituted samples is found to diminish uniformly with La content (Fig. S6*a*), following the diminishing average size of the atomic species occupying the "A" site in the perovskite lattice (Fig. S6*b*). However, locally, the atomic volume may be expected to fluctuate because lattice cavities occupied by the smaller in size La species would experience "positive" pressure from the nearby cavities occupied by the larger in size Bi atoms and shrink, and vice versa, leading to an increasing emergence of lattice distortions with La substitution. The presence of such distortions explains why the average crystallographic symmetry of La substituted samples appears diminished in comparison to pure BFO.

2.3 Large-scale structure modeling

Structure models for chemically substituted perovskites, including La substituted BFO, are difficult to explore in good detail based on crystallographic unit cells considering that some "average" atomic species occupies the same lattice sites. Therefore, to reveal the atomic structure for La substituted BFO in better detail, we constructed structure models representing 90 Å × 90 Å × 90 Å configurations of about 40 000 Fe, oxygen, Bi and La atomic species forming a perovskite lattice of the type shown in Figure 1*a* and refined

them against the respective total and Bi-differential PDFs. The initial configuration for pure BFO was generated using the PDF refined structure parameters summarized in Table S2. The large size of the atomic configurations allowed us to account for lattice distortions extending over several Bi lattice sites surrounding a guest La site, and vice versa, which is not possible if structure models constrained to a single crystallographic unit cell are employed. The refinement was done by reverse Monte Carlo (RMC) simulations using the computer program Fullrmc [56]. During the refinement, Bi, La and oxygen atoms were constrained not to approach each other closer than the Bi-O and La-O distances in $BiFeO_3$ and $LaFeO_3$ perovskites, respectively, whereas Fe-O distances were allowed to range between 1.95 Å to 2.15 Å. In addition, Fe-oxygen and oxygen-Fe first coordination numbers were restrained to stay close to six and two respectively, thus preserving the connectivity of the modelled perovskite lattice. The imposed constraints and restraints were essential to achieving physically meaningful results and never violated during the modeling. Initially, the atoms were moved with a step of 0.1 Å, which was reduced to 0.01 Å in the final stages of the modeling. It was always terminated when no further improvement in the total and Bi-differential PDF fit quality was possible to be achieved, given the particular restrains and constraints applied. Notably, three model runs for each of the studied samples were conducted. Although the atomic configurations resulted from the runs did not differ greatly, the quantities extracted from them, including the lattice polarization values reported below, were averaged over the three runs for the sake of improving the statistical accuracy of our findings. The RMC produced models fit the experimental total and Bi-differential PDF for pure and La substituted BFO in fine detail (See Fig. 6, 7 and S7). Here is to be noted that initial RMC configurations based on structure types that did not fit the experimental XRD and PDF data well could not converge to models that reproduce well the experimental PDFs either (Fig. S8). The reason is that, currently, the RMC algorithm may not necessarily adjust the lattice geometry of the initial atomic configuration, including that of the simulation box, appropriately, making it imperative to start the RMC modeling of crystal systems with local disorder from as realistic as possible initial configurations, such as, for example, configurations based on crystallographic models tested and refined by preliminary Rietveld and/or PDF analysis, as done here.

3. Discussion

It is considered that the magnitude of the spontaneous lattice polarization P_S in ferroelectric perovskites, including $LiNbO_3$, $LiTaO_3$ and BFO [57-59] is proportional to the magnitude of the "ferroelectric" displacement of Bi atoms from the geometrical center of the oxygen octahedra enclosing them (see Fig. 1*a*), where the displacement is along the $<111>_R$ direction in the perovskite lattice. Furthermore, it is considered that P_s can be conveniently evaluated using the relationship $P_s = 258*\Delta z$ ($\mu C\ cm^{-2}$), where Δz is the difference between the relative displacements of Bi and Fe atoms from their positions in a hypothetical non-ferroelectric BFO exhibiting an inversion symmetry. Here, Δz may be viewed at as a measure the

displacement of the positive charge, arising from Bi^{3+} and Fe^{3+} cations, from the negative charge, arising from O^{2-} anions, in the perovskite lattice, leading to the emergence of spontaneous electrical dipoles that order ferroelectrically in rhombohedral (S.G. *R3c*) BFO. Using this crystallographic measure for P_S and the RMC model averaged coordinates of Bi, Fe and O atoms, we obtained an average P_s value of 98 μC cm^{-2} for pure BFO, which is in line with earlier findings [57,58]. The result attests to the good quality of our structure study.

Analysis of the RMC refined structure models shows that, though distorted, the rhombohedral features of the atomic arrangement in BFO survive in the La substituted samples. This includes the asymmetry in the positioning of Bi atoms with respect to their immediate oxygen environment, which, though somewhat less expressed, is seen to persist to a La concentration as high as 40 % (see Figure 8*a*,*b*). The same is true for the presence of three types of Bi-O pairs positioned in the range of values from 2.2 Å to 2.5 Å, from 2.5 Å to 3.3 Å and from 3.3 Å to 3.6 Å (Fig. 8*c*), amounting to a Bi-oxygen coordination number of 12 (Fig. S9 [48]). Using the crystallographic measure of P_S and the relative positioning of nearby Bi and Fe species with respect to each other as computed from the respective RMC refined models (Fig. 8*d*), we evaluated the spontaneous lattice polarization in the La doped samples. The evolution of RMC model averaged P_s values with La content is summarized in Fig. 8(*h*). As can be seen in the Figure, the lattice polarization diminishes with La content but remains quite high to up to 40 % La content. Prior DFT studies also predict that it will not disappear for La content < 50 % [60-62]. Many experimental studies report that the macroscopic saturation and remnant polarization appear significantly enhanced with La content (Fig. S10 [48]) but the reported data are usually collected at different polarization fields [30,34,63,64]. Our findings agree (Fig. 8*h*) with the behavior of experimental saturation and remanent polarization data for La substituted BFO obtained when the same external electric field is applied [65,66], supporting the view that any enhancement in the macroscopic polarization of La substituted BFO would arise from a trivial increase in the phase stability of La substituted BFO and reduced leakage current and not from an increase in the lattice polarization [60].

With the replacement of Bi atoms with smaller in size La atoms, coupled rotations of Fe-O octahedra may be expected to occur because i) the size of A-type cation and octahedral rotations in perovskites are intimately coupled and ii) the Fe-O octahedra in La substituted BFO remain relatively rigid, as indicated by the small change in the Fe-O distances with La content (see Figure S6*c* [48]). Analysis of the RMC refined structure models shows that the rotations are such that the average Fe-O-Fe bond angles become closer to 180 deg (Fig. 8*e*) The increase is consistent with the observed reduction in the asymmetry in the position of Bi atoms inside the cavities between the Fe-O_6 octahedra in the perovskite lattice (see Fig. 8*a*,*b*). The magnetic properties of BFO follow the Goodenough-Kanamori rules [67] maintaining that the partially filled *d* orbitals of Fe ions will have a strong AF superexchange coupling when they form an angle of 180

deg. The observed increase in the Fe-O-Fe bond angles towards 180 deg. (Fig. 8*g*) indicates that the AF character of the exchange coupling increases with La content. This finding is consistent with the observed near linear increase in T_N for La substituted BFO [35,39] towards T_N (738 K) for the G-type antiferromagnet $LaFeO_3$ [68]. It may be expected that the observed change in the Fe-O-Fe bond angles will affect the canting of Fe magnetic moments, resulting in a small increase in the net canted moment with La content, as discussed in ref. [60]. The octahedral rotation induced by the lattice compression may also suppress the spin cycloid, as indicated by NMR experiments [69]. As a result, weak ferromagnetism may emerge and both the coercivity and remanent magnetization may increase gradually with La content, as found by us (Fig. 8*f*) and others [23,24,27,40,42,44]. Ultimately, together with the significant residual lattice polarization due to the largely preserved ferroelectric displacement of Bi atoms, this would lead to the emergence of a significant linear ME effect, as found by experiment [70]. Notably, suppressing the spin cycloid by the application of strong magnetic field also induces significant lattice distortions in rhombohedral BFO [20]. Furthermore, the suppression of the spin cycloid and emergence of a linear ME effect by reducing BFO to nanosize dimensions also involves the emergence of strong lattice distortions [21]. Altogether, lattice distortions appear central to improving the ME coupling effect in BFO.

4. Conclusions

The partial substitution of Bi by nonmagnetic La in $BiFeO_3$ induces compressive lattice strain which distorts the crystal lattice such that the average lattice symmetry is reduced to triclinic but the rhombohedral symmetry relationship between the positions of constituent atoms is largely preserved. As such, the atomic structure of La substituted BFO appears difficult to comprehend in traditional crystallographic terms. For the purposes of exploring the interaction between the ferroic orders exhibited by the system, the structure can be described by models refined against atomic PDFs, giving the most probable positions of atoms in the studied material. The PDF-guided RMC modeling conducted here indicates that the coherence of the ferroelectric displacements of Bi^{3+} species in $Bi_{1-x}La_xFeO_3$ ($0 \leq 0.4$) is preserved to a great extent and, hence, though weakened, the cooperative ferroelectricity is also preserved, as shown by numerous experiments. At the same time, the Fe-O_6 octahedra rotate such that, regardless the overall AF order strengthens, macroscopic magnetization emerges likely due to an increase in the spin canting angle and/or suppression of the Fe spin cycloid. This is a vivid demonstration of the interaction between electrical, magnetic and lattice degrees of freedom in a strongly correlated system where the latter appear as local lattice distortions entangling the former.

ACKNOWLEDGMENTS

This work was supported by the U.S. Department of Energy, Office of Science, Office of Basic Energy Sciences under Award No. DE-SC0021973 and used resources of the Advanced Photon Source at the

Argonne National Laboratory provided by the DOE Office of Science under Contract No. DE-AC02-06CH11357. The help of Dr. T. Durga in preparing the samples is greatly appreciated.

References

[1]. M. Fiebig, Th. Lottermoser, D. Meier, and M. Trassin, Nat. Rev. Mater. **1**, 16046 (2016).
[2] D. Khomskii, Physics **2**, 20 (2009).
[3] R. Ramesh and N. A. Spaldin, Nat. Mater. **6**, 21-29 (2007).
[4] S.-W. Cheong and M. Mostovoy, Nat. Mater. **6**, 13 (2007).
[5] N. Spaldin, S.-W. Cheong, and R. Ramesh, Phys. Today **63**(10) (2010).
[6] J.-T. Han, Y.-H. Huang, X.-J. Wu, C.-L. Wu, W. Wei, B. Peng, W. Huang, and J. B. Goodenough, Adv. Mater. **18**, 2145 (2006).
[7] S. V. Kiselev, R. P. Ozerov, and G. S. Zhdanov, Sov. Phys. Dokl. **7**, 742 (1963).
[8] I. H. Lone, J. Aslam, N. R. E. Radwan, A. H. Bashal, A. F. A. Ajlouni, and A. Akhter, Nano Res. Lett. **14**, 142 (2019).
[9] Y. Yin and Q. Li, J. Materiomics **3**, 245 (2017).
[10] J. Park, S.-H. Lee, S. Lee, F. Gozzo, H. Kimura, Y. Noda, Y. J. Choi, V. Kiryukhin, S.-W. Cheong, Y. Jo, E. S. Choi, L. Balicas, G. S. Jeon, and J.-G. Park J. Phys. Soc. Jap. **80**, 114714 (2011).
[11] M. Ramazanoglu, M. Laver, W. Ratcliff II, S. M. Watson, W. C. Chen, A. Jackson, K. Kothapalli, S. Lee, S.-W. Cheong, and V. Kiryukhin Phys. Rev. Lett. **107**, 207206 (2011).
[12] A. Palewicza, I. Sosnowska, R. Przeniosło, and A. W. Hewat, Acta Phys. Pol. A **117**, 296 (2010).
[13] U. Nuraini and S. Suasmoro, J. Phys.: Conf. Ser. **817**, 012059 (2017).
[14] H. D. Megaw and C. N. W. Darlington, Acta Crystallogr., Sect. A **31**, 161 (1975).
[15] A. J. Jacobson and B. E. F. Fender, J. Phys. C: Solid State Phys. **8**, 844 (1975).
[16] N. V. Srihari, K. B. Vinayakumar, and K. K. Nagaraja, Coatings **10**, 1221 (2020).
[17] S. Kawachi, S. Miyahara, T. Ito, A. Miyake, N. Furukawa, J. I. Yamaura, and M. Tokunaga, Phys. Rev. B **100**, 140412 (2019).
[18] A. Agbelele, D. Sando, C. Toulouse, C. Paillard, R. D. Johnson, R. Rüffer, A. F. Popkov, C. Carrétéro, P. Rovillain, J.-M. Le Breton, B. Dkhil, M. Cazayous, Y. Gallais, M.-A. Méasson, A. Sacuto, P. Manuel, A. K. Zvezdin, A. Barthélémy, J. Juraszek, and M. Bibes, Adv. Mater. **29**, 1602327 (2017).
[19] M. D. Davydova, K. A. Zvezdin, A. A. Mukhin, and A. K. Zvezdin, Phys. Sci. Rev. **5**, 20190070 (2020).
[20] T. Room, J. Viirok, L. Peedu, U. Nagel, D. G. farkas, D. Szaller, V. Kocsis, S. Bordacs, I. Kezsmarki, D. L. Kamenskyi, H. Engelkamp, M. Oxzeorv, D. Smirnov, J. Krzystek, K. Thirunavukkuarasu, Y. Ozaki, Y. Tomioka, T. Ito, T. Datta, and R. S. Fishman Phys. Rev. B **102**, 214410 (2020).
[21] V. Petkov and S. Shastri Phys. Rev. B **104**, 054121 (2021).
[22] D. C. Arnold IEEE Trans. On Ultrasonics, Ferroelectrics and Frequency Control **62**, (2015).
[23] Y.-Jie Zhang, H.-Guo Zhang, J.-Hua Yin, H.-Wei Zhang, J.-Ian Chen, W.-Quan Wang, and G.-Heng Wu J. Mag. Magn. Mater. **322**, 2251 (2010).
[24] F. Mumtaz, S. Nasir, G. H. Jaffari, and S. I. Shah J. Alloys. Comp. **876**, 160178 (2021).
[25] J. Dong, X. Zhang, Y. Wang, Y. Gong, P. An, H. Li, Z. Guo, X. Hao, Q. Jia, and D. Chen J. Phys.: Condens. Matter **31**, 085402 (2019).
[26] M. Polomska, W. Kaczmarek, and Z. Pająk Phys. Stat. Sol. A **23**, 567 (1974).
[27] M. Polomska, B. Hilczer, I. Szafraniak-Wiza, A. Pietraszko, and B. Andrzejewski Phase Trans. **90**, 24 (2017).
[28] J. Wei, Ch. Wu, Y. Liu, Y. Guo, T. Yang, D. Wang, Z. Xu, and R. Haumont Inorg. Chem. **56**, 8964 (2017).
[29] S. Karimi, I. M. Reaney, Y. Han, J. Pokorny and I. Sterianou J. Mater. Sci. **44**, 5102 (2009).
[30] Z. Chen, Y. Li, Y. Wu, and J. Hu J. Mater Sci: Mater Electron **23**, 1402 (2012).

[31] Y. Horibe, M. Nomoto, T. Inoshita, K. Watanabe, S.-W. Cheong, Y. Inoue, and Y. Koyama Phys. Rev. B **100**, 024105 (2019).
[32] A. Kumar and D. Varshney J. Electronic Mater. **44**, 4354 (2015).
[33] P. Chen, O. G.-Sen, W.J. Ren, Z. Qin, T. V. Brinzari, S. McGill, S.-W. Cheong, and J.L. Musfeldt Phys. Rev. B **86**, 014407 (2012).
[34] R. Rai, S. K. Mishra, N. K. Singh, S. Sharma, and A. L. Kholkin Current Appl. Phys. **11**, 508 (2011).
[35] P. Thakuria and P. A. Joy Solid State Comm. 152, 1609 (2012).
[36] J. A. M. Cagigas, D. S. Candela, and E. Baggio-Saitovitch J. Phys.: Conf. Ser. **200**, 012134 (2010).
[37] J. Chen, R. Yu, L. Li, C. Sun, T. Zhang, H. Chen, and X. Xing Eur. J. Inorg. Chem. 2008, 3655.
[38] J. A. Dean Lange's Handbook of Chemistry 15th ed. McGraw Hill, New York 1999.
[39] Z.V. Gabbasova, M.D. Kuz'min, A.K. Zvezdin, I.S. Dubenko, V.A. Murashov, D.N. Rakov, and I. B. Krynetsky Phys. Let A **158**, 491 (1991).
[40] D. A. Rusakov, A. M. Abakumov, K. Yamaura, A. A. Belik, G. van Tendeloo, and E. Takayama-Muromachi Chem. Mat. **23**, 285 (2011).
[41] I. O. Troyanchuk, D.V. Karpinsky, M.V. Bushinsky, O. S. Mantytskaya, N. V. Tereshko, V. N. Shut, J. Am. Ceram. Soc. **94**, 4502 (2011).
[42] I. O. Troyanchuk, M. V. Bushinsky, D. V. Karpinsky, O. S. Mantytskaya, V. V. Fedotova, and O. I. Prochnenko Phys. Stat. Sol. B 246, 1901 (2009).
[43] T.T. Carvalho, J.R.A. Fernandes, J. Perez de la Cruz, J.V. Vidal, N.A. Sobolev, F. Figueiras, S. Das, V.S. Amaral, A. Almeida, J. A. Moreira, and P. B. Tavares J. Alloys Comp. **554**, 97 (2013).
[44] M. M. Gomes, T. T. Carvalho, B. Manjunath, R. Vilarinho, A. S. Gibbs, K.S. Knight, J.A. Paixao, V. S. Amaral, A. Almeida, P. B. Tavares, and J.A. Moreira Phys. Rev. B **104**, 174109 (2021).
[45] P. Juhás, T. Davis, C. L. Farrow and S. J. L. Billinge J. Appl. Crystallogr. **46**, 560 (2013).
[46] V. Petkov and V. Buscaglia Phys. Rev. Mat. **5**, 044410 (2021).
[47] V. Petkov, J. W. Kim, S. Shastri, S. Gupta, and S. Priya Phys. Rev. Mater. **4**, 014405 (2020).
[48] Supplemental Material
[49] V. Petkov J. Appl. Cryst. **22** (1989) 387.
[50] Y. Waseda, in *Novel Applications of Anomalous (Resonance) X-ray Scattering for Characterization of Disordered Materials*. Berlin: Springer (1984).
[51] V. Petkov and S. Shastri Phys. Rev. B **81**, 165428 (2010).
[52] V. Petkov, S. Shastri, J.-Woo Kim, S. Shan, J. Luo, J.Wu and C.-J. Zhong Acta Cryst. A **74**, 553 (2018).
[53] J. Rodriguez-Carvajal, Commission on Powder Diffraction (IUCr) Newsletter **26**, 12 (2001).
[54] H. Wang, Ch. Yang, J. Lu, M. Wu, J. Su, K. Li, J. Zhang, G. Li, T. Jin, T. Kamiyama, F. Liao, J. Lin, and Y. Wu Inorg. Chem. **52**, 2388 (2013).
[55] C. L. Farrow, P. Juhás, Jiwu Liu, D. Bryndin, E. S. Bozin, J. Bloch, Th. Proffen and S. J. L. Billinge J. Phys: Condens. Mat. **19**, 335219 (2007)
[56] B. Aoun J. Appl. Cryst. **55**, 1664 (2022).
[57] J. B. Neaton, C. Ederer, U. V. Waghmare, N. A. Spaldin, and K. M. Rabe Phys. Rev. B **71**, 014113 (2005).
[58] P. Ravindran, R. Vidya, A. Kjekshus, H. Fjellvåg, and O. Eriksson Phys. Rev. B **74**, 224412 (2006).
[59] S. C. Abrahams, S. K. Kurtz, and P. B. Jamieson Phys Rev. **172**, 551 (1968).
[60] J.-H. Lee, H. J. Choi, D. Lee, M. G. Kim, C. W. Bark, S. Ryu, M.-A. Oak, and H. M. Jang Phys. Rev. B **82**, 045113 (2010).
[61] E-Aguilar, H´Linh Hmŏk, and J. M. Siqueiros Mat. Res. Express **6**, 085098 (2019).
[62] A. Ghosh, D. P. Trujillo, H. Choi, S.M. Nakhmanson, S. P. Alpay, and J.-X Zhu Sci. Rep. **9**:194 (2019).
[63] P. Trivedi, S. Katba, S. Jethva, M. Udeshi, B. Vyas, M. Vagadia, S. Gautam, K. H. Chae, K. Asokan, and D.G. Kuberkar Soli. State. Comm. **222**, 5 (2015).
[64] L. Peng-Ting, L. Xiang, Z. Li, Y. Jin-Hua, C. Xing-Wang, W. Zhi-Hong, W. Yu-Chuan, and

W. Guang-Heng Chin. Phys. B **23**, 047701 (2014).
[65] S. T. Zhang, L.-H. Pang, Y. Zhang, M.-H. Lu, and Y.-F. Chen J. Appl. Phys. 100, 114108 (2006).
[66] S. T. Zhang, Y. Zhang, M.-H. Lu, C.-L. Du, Y.-F. Chen, Z.-G. Liu, Y.-Y. Zhu, and N.-B. Ming Appl. Phys. Lett. **88**, 162901 (2006).
[67] H. Weihe and H. U. Gudel Inorg. Chem. **36**, 3632 (1997).
[68] S. M. Selbach, J. R. Tolchard, A. Fossdal, and T. Grande J. Sol. State Chem. **196**, 249 (2012).
[69] A. V. Zalesskii, A. A. Frolov, T. A. Khimich, and A. A. Bush Phys. Solid. State **45**, 141 (2003).
[70] A. A. Amirov, I. K. Kamilov, D. M. Yusupov, L. A. Reznichenko, O. N. Razumovskaya, and I. A. Verbenko Phys Procedia **75**, 10 (2015).

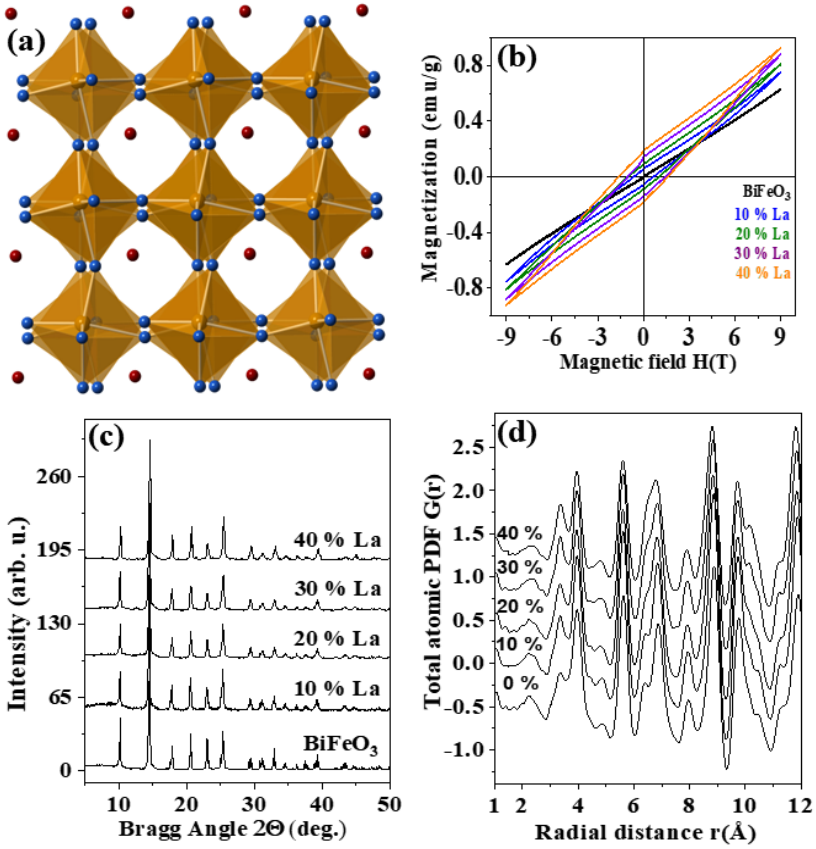

Figure 1. (*a*) Fragment from the rhombohedral structure of $BiFeO_3$ projected down the $<001>_R$ direction, featuring corner shared Fe (brown circles)–oxygen (blue circles) octahedra with Bi (red circles) atoms positioned in the cavities between them. The octahedra are rotated with respect to each other and and Bi atoms are displaced from the geometrical center of the cavities, rendering the material ferroelectric. (*b*) XRD patterns, (*c*) room temperature hysteresis curves and (*d*) total atomic PDFs G(r) for pure and La substituted $BiFeO_3$. The PDFs are offset vertically for clarity.

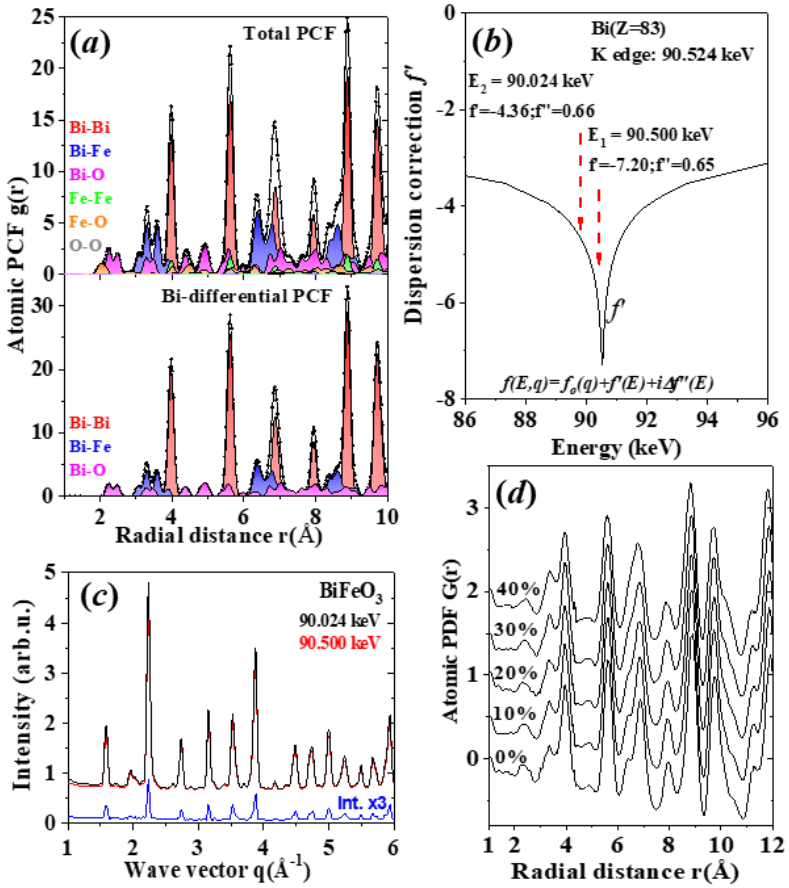

Figure 2. (*a*) Computed total and Bi-differential atomic pair correlation functions (PCFs) g(r) (black) for pure $BiFeO_3$. The individual partial PCFs are also shown, each in a different color. (*b*) Energy dependence of the real dispersion correction *f'* for Bi. The energies below the K edge of Bi used in the present experiments are marked with arrows. Values for *f'* and *f''* at these energies are also given. (*c*) XRD patterns for $BiFeO_3$ taken and at 25 eV (red) and 500 eV (black) below the K edge of Bi (90.524 keV). Their difference (blue), multiplied by a factor of 3 and shifted by subtracting a constant factor for clarity is also given. (*d*) Experimental Bi-differential atomic PDFs G(r) for pure and La substituted $BiFeO_3$. The PDFs are offset vertically for clarity. Note that, as defined, the PCF $g(r)=\rho(r)/\rho_o$, oscillates about one while the PDF $G(r)=4pr\rho_o[\rho(r)-1]$ oscillated about zero. Here $\rho(r)$ and ρ_o are the local and average atomic number density, respectively.

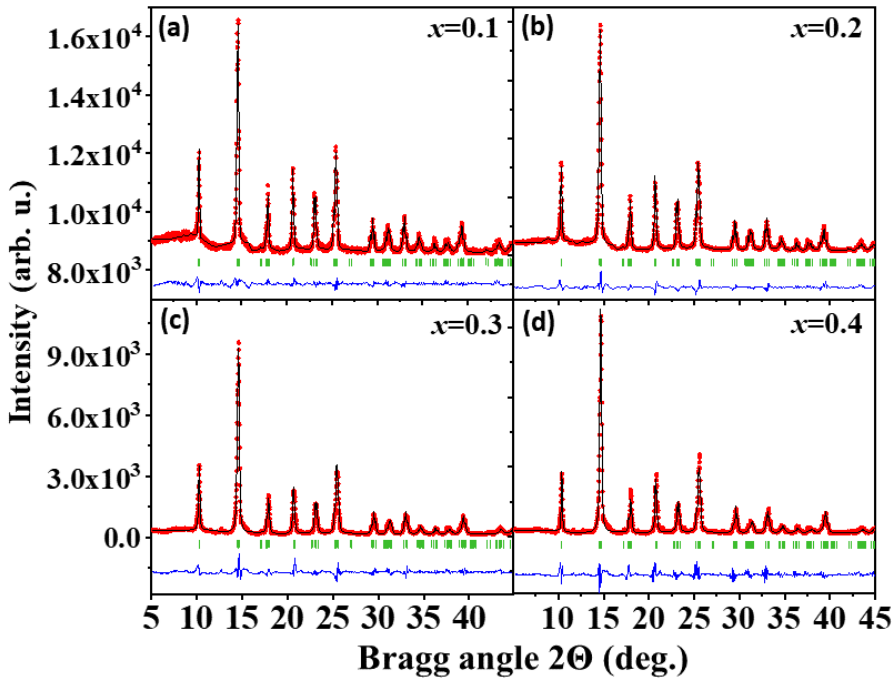

Figure 3. Rietveld fits (black) to XRD patterns (red) for La substituted $Bi_{1-x}La_xFeO_3$ based on a S.G. *R3c* model. Vertical green bars show the position of Bragg peaks. The residual difference (blue) is shifted by subtracting a constant for clarity. The goodness-of-fit indicator, R_{wp}, is about 6 % for the x=0.1 and x=0.2 samples. It is about 13 % and 16 % for the x=0.3 and x=0.4 samples, respectively.

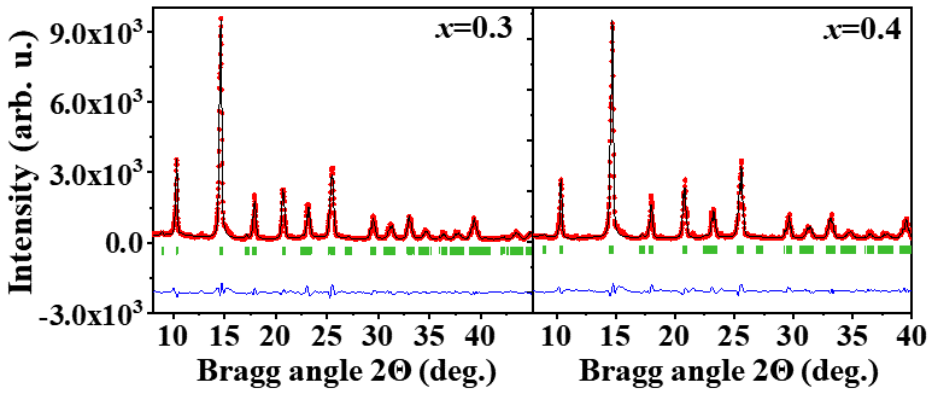

Figure 4. Rietveld fits (black) to XRD patterns (red) for La substituted $Bi_{1-x}La_xFeO_3$ based on a S.G. *P1* model. Vertical green bars show the position of Bragg peaks. The residual difference (blue) is shifted by subtracting a constant for clarity. The goodness-of-fit indicator, R_{wp}, is about 7 % and 9 % for the x=0.3 and x=0.4 samples, respectively.

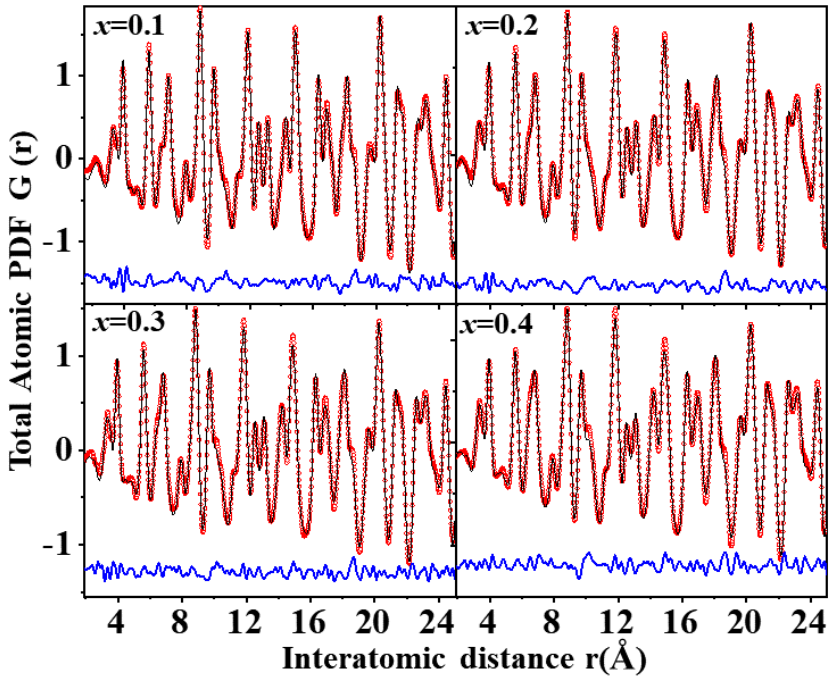

Figure 5. Crystallographic (small unit cell) fits (black) to experimental PDFs G(r) (red) for La substituted $Bi_{1-x}La_xFeO_3$ based on a S.G. *P1* model. The residual difference (blue) is shifted by subtracting a constant for clarity. The goodness-of-fit indicator, R_{wp}, is for the fits is about 13 %.

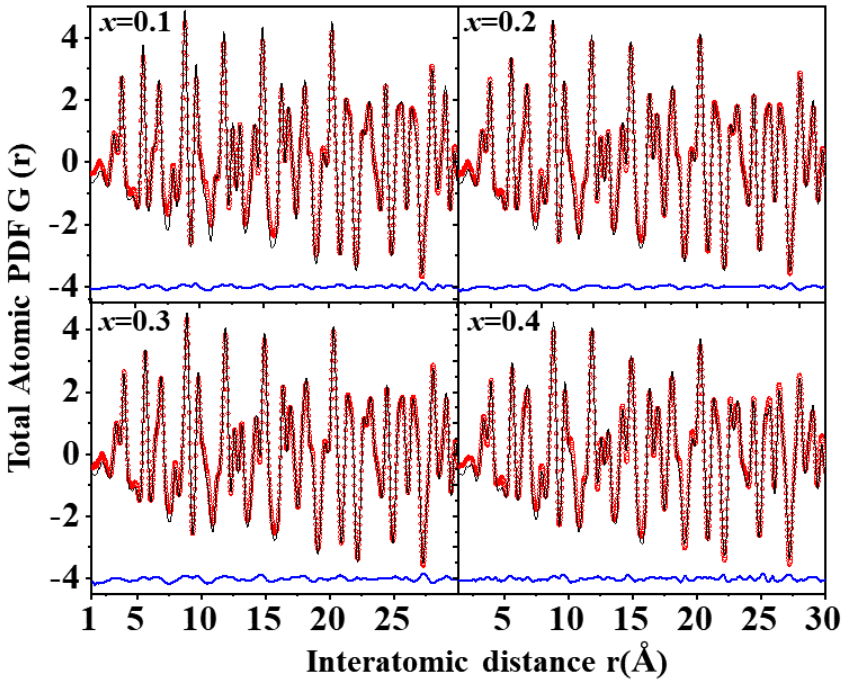

Figure 6. RMC (large model based) fits (black) to experimental PDFs G(r) (red) for La substituted $Bi_{1-x}La_xFeO_3$. The initial configuration is based on a S.G. *P1* type structure. The residual difference (blue) is shifted by subtracting a constant for clarity. The goodness-of-fit indicator, R_{wp}, for the fits is about 6 %.

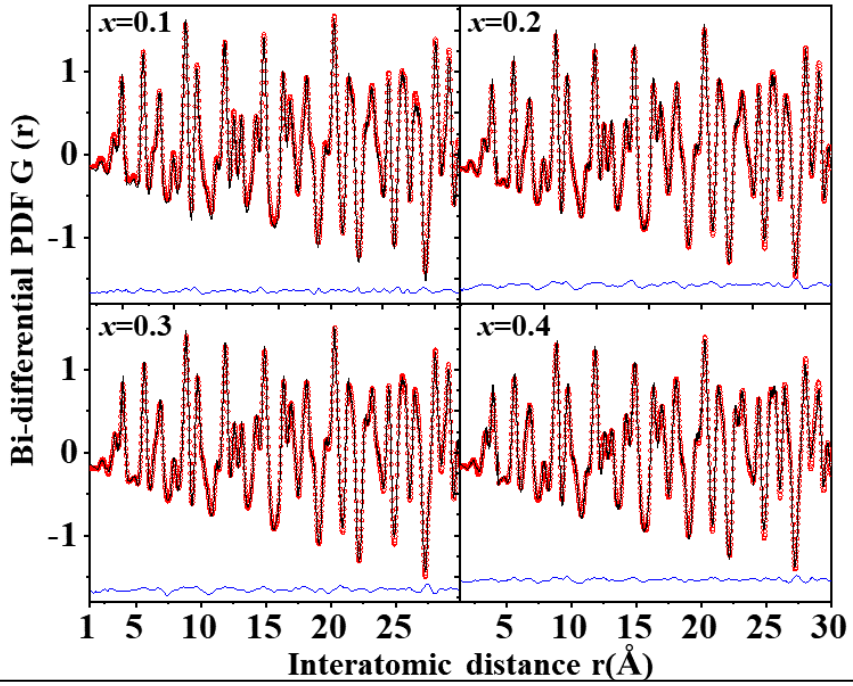

Figure 7. RMC (large model based) fits (black) to experimental Bi-differential PDFs G(r) (red) for La substituted $Bi_{1-x}La_xFeO_3$. The initial configuration is based on a S.G. *P1* type structure. The residual difference (blue) is shifted by subtracting a constant for clarity. The goodness-of-fit indicator, R_{wp}, for the fits is about 6 %.

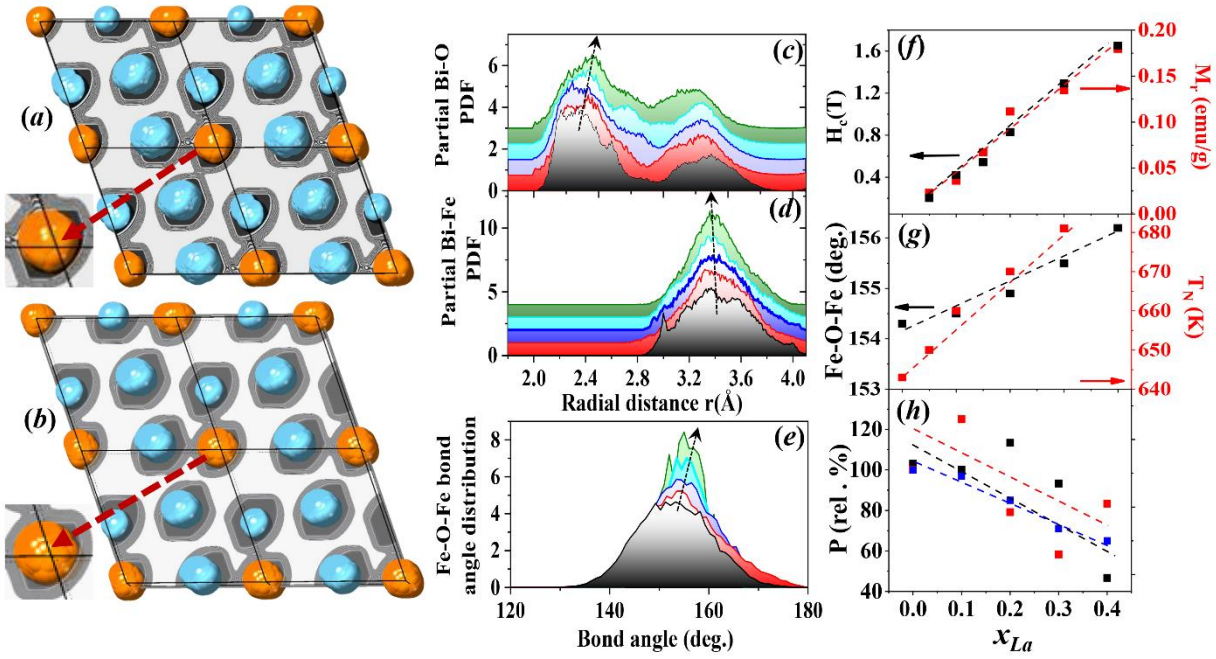

Figure 8. Projection of the RMC refined model for (a) $BiFeO_3$ and (b) $Bi_{0.6}La_{0.4}FeO_3$ onto the $(001)_R$ atomic plane of the perovskite lattice. For simplicity, Fe atoms are not shown. Bi atoms are in brown and oxygen atoms are in blue. The gray shaded contour boundaries include 99 % of all atoms at the particular lattice sites. The blue/orange-colored regions include all atoms at the particular site, where atoms that are closer than 0.5 Å are merged. Bi atoms in $Bi_{0.6}La_{0.4}FeO_3$ appear less displaced from the geometrical centers of the oxygen polyhedron that encloses them in comparison to Bi atom in pure BFO (Compare the positions of the crosshair-type projection of the unit cell edges on the distribution of Bi atoms at the center of the plots, which, for clarity, is also shown enlarged on their left side). Partial (c) Bi-O and (d) Bi-Fe PDFs G(r) computed from the RMC refined models for $Bi_{1-x}La_XFeO_3$ (x=0, 0.1, 0.2, 0.3 and 0.4). (e) Distribution of Fe-O-Fe bond angles computed from the RMC models; (f) Our experimental data for the coercive field, H_c, and remanent magnetization, M_r for pure and La substituted BFO. (g) RMC model averaged Fe-O-Fe bond angles (black) and experimental Neel temperature T_N (red) for La substituted BFO (h); Change in computed spontaneous (blue) and experimental saturation (red) and remnant (black) polarization in La substituted BFO. Broken lines in (f), (g) and (h) are a guide to the eye. Arrows in (c), (d) and (e), highlight trends in the shown data sets with increasing La content, x_{La}, from x=0 (black) to x=0.4 (green).